

Numerical simulation of atmospheric bore waves on Mars

Magdalena R.V. Sta. Maria^{a,*}, Scot C.R. Rafkin^b, Timothy I. Michaels^b

^a Department of Civil and Environmental Engineering, Terman Engineering Center M42, Stanford University, Stanford, CA 94305, USA

^b Southwest Research Institute, 1050 Walnut St., Suite 400, Boulder, CO 80302, USA

Received 25 July 2005; revised 6 July 2006

Available online 18 September 2006

Abstract

The Viking Orbiters imaged early morning, long, linear wave clouds along the flanks of the Tharsis volcanoes during late northern spring and early summer. These clouds are believed to be a product of either an atmospheric bore wave or a hydraulic jump generated by nightly katabatic winds. The Mars Regional Atmospheric Modeling System was used to study the interaction of the katabatic flows with the surrounding atmosphere to determine what mechanism is responsible for the clouds. Simulations at $L_s = 90^\circ, 100^\circ, 142^\circ, 180^\circ, 270^\circ,$ and 358° were conducted focusing on the eastern flank of Olympus Mons. Model results compare well with Viking observations and closely approximate theoretical treatments of atmospheric bores. Strong downslope flows are simulated during the night, with a bore wave forming on and behind a well-defined katabatic front. The observed seasonality of the clouds was reproduced in the simulations; the bore was deeper and faster during northern summer and weakest during the winter. When the bore was strong, it was undular in form, and generated vertically propagating gravity waves in the atmosphere above. During the winter, the atmospheric structure was such that any gravity waves generated damped with height. Less atmospheric water vapor abundance during northern winter, as compared to the summer, is also a factor in the seasonality of the wave clouds. This study concludes that bore waves are the most likely mechanism for the generation of the observed linear wave clouds.

© 2006 Elsevier Inc. All rights reserved.

Keywords: Mars, atmosphere; Meteorology; Atmospheres, dynamics; Atmospheres, structure

1. Introduction

The Viking Orbiters imaged long rolling wave clouds (Briggs et al., 1977; Hunt et al., 1981) along the flanks of the Tharsis volcanoes almost three decades ago (Fig. 1). In the two years that the Viking Orbiters observed Mars, these clouds were only seen in the early morning during the late northern spring and early northern summer, and dissipated by approximately 1000 local time.

Two hypotheses for the origin of the observed cloud phenomenon have been suggested. Kahn and Gierasch (1982) favored a hydraulic jump explanation in which katabatic drainage flows originating from the volcano slopes and moving at a speed greater than the internal gravity wave speed, propagate into the undisturbed, ambient air at the foot of the volcanoes. As a result, a shockwave or fluid field discontinuity (i.e., a hydraulic

jump) is produced at the katabatic front. It was suggested that waves originate at the hydraulic jump and generate the linear cloud structures. Hunt et al. (1981) and Pickersgill (1984) preferred a slightly different idea, although they also cite the katabatic drainage flows from the volcanoes as the catalyst for these disturbances. Pickersgill compared the martian clouds to the “Morning Glory” clouds, seen off the coast of Carpentaria, Australia (Clarke, 1972), which are caused by atmospheric bores, and suggested that the martian clouds were a result of bores generated by a katabatic front.

The difference between the mechanisms proposed by Kahn and Gierasch (1982), and Hunt et al. (1981) and Pickersgill (1984) may be more a matter of semantics than true differences in physics. The literature is full of examples where the terms bores and hydraulic jump are used somewhat interchangeably (e.g., Rottman and Simpson, 1989). However, others make a distinction between the two. For example, Klemp et al. (1997) indicates that, “Shocks propagating into a quiescent fluid are typically called bores, while flows decelerating through a nearly stationary shock are termed hydraulic jumps.” To some degree,

* Corresponding author.

E-mail address: eena@stanford.edu (M.R.V. Sta. Maria).

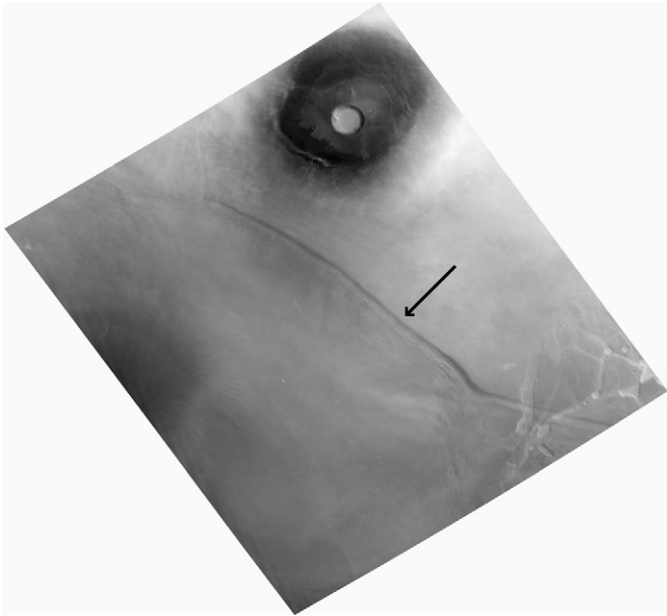


Fig. 1. Long, linear wave clouds observed between Pavonis and Arsia Mons by Viking Orbiter. The arrow indicates the most pronounced cloud feature. Pavonis Mons is in the image; the east slope of Arsia is the dark region on the west side of the image.

the distinction or blurring thereof may be caused by differences in a frame of reference, since “nearly stationary” clearly depends on a frame of reference. In this paper, “stationary” is taken to mean in a frame of reference with respect to the ground. However, it is also possible to use the motion of the obstacle triggering the bore to be the frame of reference; this is often convenient for theoretical treatments. In this case, if the “bore” moves at the same speed as the triggering obstacle, then it should properly be considered a “hydraulic jump.” To further complicate matters, the bore or hydraulic jump may form in an atmospheric environment with substantial velocity. In this case, it is not clear whether to choose a reference frame associated with the non-moving ground, the moving obstacle triggering the bore, or the atmospheric flow. This study presents mesoscale modeling results that show the production of katabatically-generated waves along the slopes of Olympus Mons. If the frame of reference is the ground—as in this paper—the waves are produced by a bore, since the bore propagates into an unperturbed (but moving) environment.

2. Bore theory and observations

2.1. Theory

A bore is a solitary wave that propagates (with respect to the ground) along a density interface as shown schematically in Fig. 2. Here, there is a motionless fluid of density ρ_0 with an undisturbed depth of h_0 underlying a less dense, motionless fluid of density ρ_1 and depth $H - h_0$. A third fluid (shaded region, ρ_g), with the greatest density, intrudes into the bottom layer at speed U , generating a propagating disturbance known as a bore, moving at speed U_b . The bore speed is usually greater than the current speed, U , and is driven by the momentum of the

Idealized Schematic of a Bore

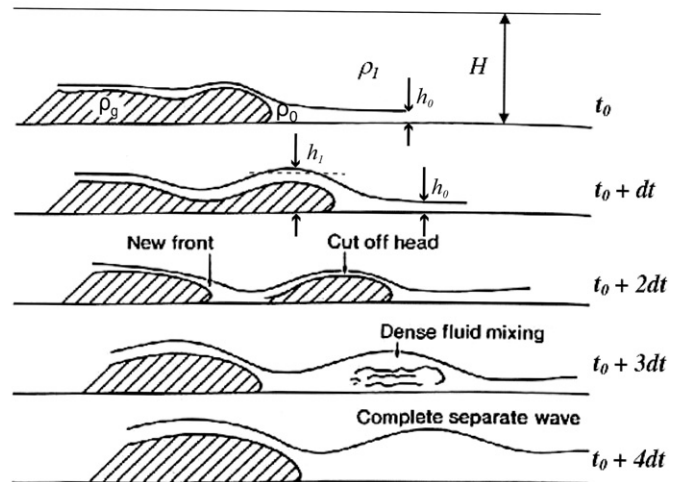


Fig. 2. Idealized schematic of how a bore forms from a density current (stippled region) intruding into a fluid with two layers of lower density (reference for original figure unknown). See text for details.

undisturbed fluid colliding with the impinging density current. The depth H is assumed to be much deeper than h_0 , and the disturbance does not perturb the height of the upper fluid, which remains at height H .

In the reference frame of advancing current, the undisturbed fluid appears to be impinging on an obstacle comprised of the dense current. The ratio of the kinetic energy (per unit mass) of the undisturbed fluid speed U (in the reference frame of the advancing current) to the gravitational potential energy (per unit mass) of the undisturbed fluid is known as the Froude number:

$$Fr = \frac{U^2}{g'h_0}, \quad (1)$$

where $g' = g(\rho_0 - \rho_1)/\rho_0$ is the reduced gravity, and g is gravitational acceleration. Alternatively, the denominator of Eq. (1) is the square of the shallow water gravity wave speed, so that Fr can be viewed as the square of the ratio of the fluid velocity to the internal gravity wave speed. If $Fr \leq 1$, gravity waves forced by a disturbance can propagate ahead (upstream) of the obstacle. If $Fr > 1$, gravity waves may not propagate faster than (ahead of) the fluid. Importantly, the Froude number may change as the flow interacts with the obstacle and the depth and speed of the fluid changes.

Not all density currents produce bores. The criteria for generation of a bore from a density current is a function of the Froude number in the undisturbed fluid and the relative heights of the current (d_0) and undisturbed fluid, h_0 (Klemp et al., 1997) as shown in Fig. 3 (their Fig. 18). The height of the undisturbed fluid can be related to the height of an inversion—the stronger the inversion, the larger the h_0 —and the height of the current depends on the scale of the gravity current source. At relatively high Froude numbers and comparatively low d_0/h_0 , there is sufficient kinetic energy in the undisturbed flow, as seen from the reference frame of the advancing density current, to overcome the potential energy of the barrier (i.e., the density current), and the bulk of the undisturbed fluid flows over the

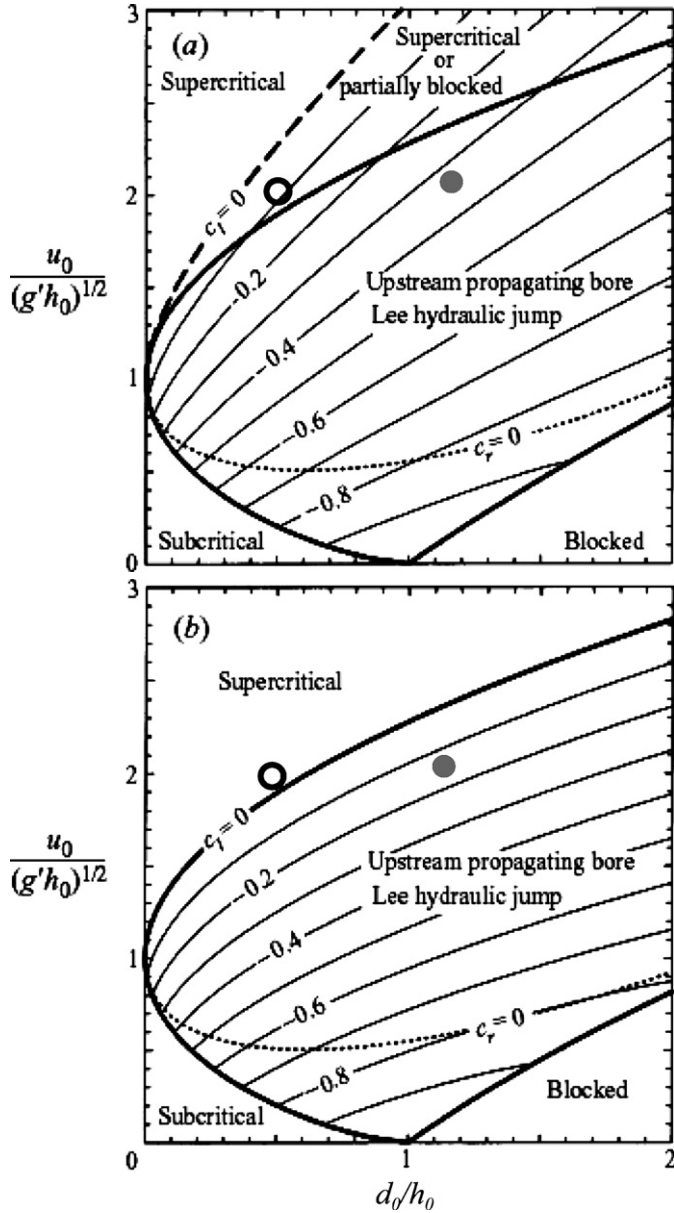


Fig. 3. This plot from Klemp et al. (1997) shows the flow regimes based on the Froude number and the ratio of the density current head (d_0) to the undisturbed fluid (h_0). Depending on these two parameters, the flow is either supercritical, subcritical, partially blocked or completely blocked. Bores are generated when the flow is either partially or completely blocked. The thin, solid lines indicate the speed of the bore. The dotted line separates the regimes for downstream-propagating lee hydraulic jumps (above) and stationary hydraulic jumps (below). (a) A plot based on Houghton and Kasahara (1968), where traditional hydraulic theory (conservation of mass and momentum) is applied to upstream propagating bores. (b) Modified version of (a) assuming that energy, instead of mass and momentum, is conserved within the shallow water layer through which the bore is propagating. Based on the modeling results, the approximate flow regime at $L_s = 100^\circ$ is indicated by the filled dot. The open dot shows the approximate regime at $L_s = 358^\circ$.

obstacle, accelerating and thinning as it passes over the crest and returning to the undisturbed state on the lee side. The flow is said to be supercritical, and there is no disturbance ahead or behind the obstacle in this case. As the ratio d_0/h_0 grows or Fr decreases in the undisturbed fluid, the flow may not have sufficient kinetic energy to completely overcome the barrier. In

such a case the flow is partially blocked, and a fluid discontinuity propagating into the undisturbed fluid (i.e., a bore) can develop ahead of the obstacle. For $Fr < 1$ and $d_0/h_0 < 1$, this regime is mostly defined to be subcritical, and, like supercritical flow, there is no disturbance. For low Fr (e.g., $Fr < 0.8$) flows and large barrier-to-fluid height ratios ($d_0/h_0 > 1$), the flow is completely blocked and all the fluid is pushed ahead of the obstacle. Bores are generated when the flow regime is defined to be partially blocked (the striped region in Fig. 3).

The strength of a bore is gauged by the ratio h_1/h_0 , where h_1 is the mean height of the bore. Rottman and Simpson (1989) classified bores into three regimes based on laboratory studies. In these studies, an obstacle is towed through a tank of undisturbed, motionless fluids; Fig. 4 shows the three types of bores generated. A smooth, undular bore forms with $1 < h_1/h_0 < 2$, and there is little or no mixing along the interface between fluids of density ρ_0 and ρ_1 (Fig. 4a). “Undular” refers to the wave-train trailing the bore interface. When $2 < h_1/h_0 < 4$, the bore is also mostly undular, though more mixing (turbulence) is observed along the interface (Fig. 4b). For $h_1/h_0 > 4$ the bore appears similar to a gravity current, with turbulent mixing behind the leading edge overwhelming any undulations that may form (Fig. 4c). Undular (weak) bores were found to propagate with a speed governed by

$$\frac{C^2}{g'h_0} = \frac{1}{2} \frac{h_1}{h_0} \left(1 + \frac{h_1}{h_0} \right), \quad (2)$$

where C is the bore speed (U_b). The bore speed for stronger bores, i.e., when $h_1/h_0 > 2$, is governed by the following empirical formula (Huppert and Simpson, 1980):

$$\frac{C^2}{g'h_0} = 1.19. \quad (3)$$

Note that the l.h.s. of both Eqs. (2) and (3) is the Froude number. Since bore strengths are defined for h_1/h_0 greater than 1, the Froude number is greater than 1 in Eq. (2), and is defined as such for Eq. (3). This implies that the propagation speed of bores exceeds the gravity wave speed, as noted by Kahn and Gierasch (1982).

In linear shallow water theory, bore disturbances are found by considering a steady-state solution. However, in reality, bores undergo a life cycle as illustrated in Fig. 2. An undular bore generated in a laboratory tank (Rottman and Simpson, 1989) begins as a smooth hump in the fluid of density ρ_0 , as it flows over the head of the density current (at time t_0 in Fig. 2). The undisturbed flow is partially blocked as the current impinges on it, and because of this there is an induced velocity component in the undisturbed fluid that is in the direction of the density current propagation. The bore develops as the hump then detaches from the main current, and moves ahead of the dense air mass due to the induced velocity in the partially blocked undisturbed fluid (at time $t_0 + 2dt$). In some instances, the hump may cause some of the denser fluid to detach from the bulk of density current. However, a new hump redevelops at the leading edge of the density current, and the process repeats itself. The result of this process is a series of wave-like oscillations downstream

Laboratory Images of Different Bore Types

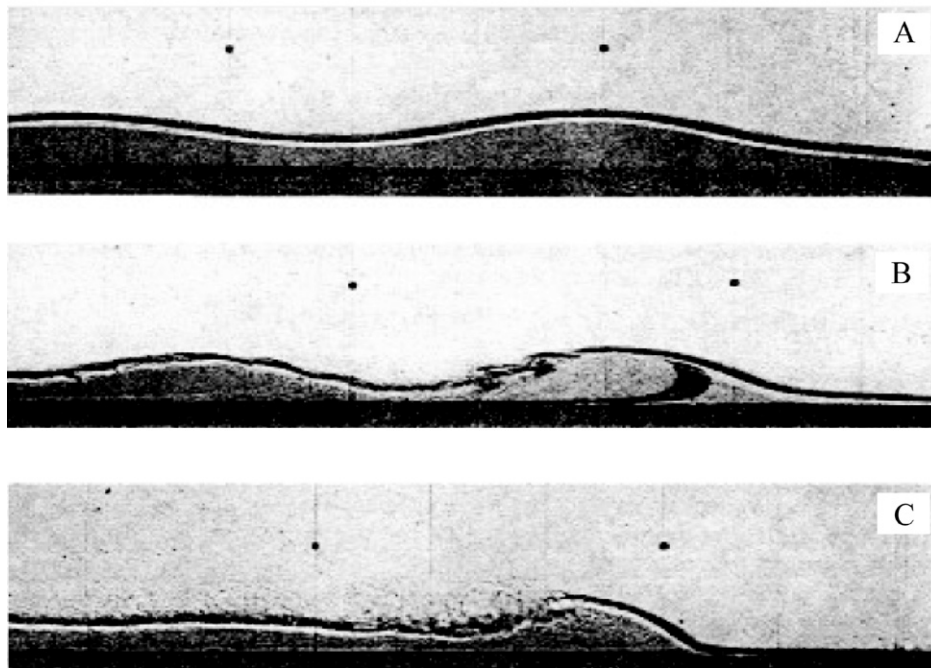


Fig. 4. Laboratory photographs (from Rottman and Simpson, 1989) of three bores with different strengths: (A) $1 < h_1/h_0 < 2$ (undular), (B) $2 < h_1/h_0 < 4$ (mostly undular), and (C) $h_1/h_0 > 4$ (turbulent). Note here the difference in height of the fluid in front of the propagating bore wave, with (C) showing the shallowest h_0 .

(ahead) of the density current propagating along the interface of fluids 1 and 2, at speed U_b (Rottman and Simpson, 1989; Holyer and Huppert, 1980).

In the natural environment, bores have been observed to occur both in water and in the atmosphere. The atmosphere, however, is typically not as simple a system as the three-fluid systems shown in Figs. 2 and 4. Other processes come into play in the atmosphere. For example, the atmosphere is typically not motionless like the undisturbed fluids in laboratory studies. Also, the bore's passage can excite vertically propagating gravity waves, because the atmosphere is continuously stratified. Fig. 5 shows a schematic of a bore observed on Earth. Drawn from terrestrial meteorological station data, the plot is a time series of the passage of a bore generated by a dissipating thunderstorm gust front. Assuming the bore structure is in steady state as it propagates, the temporal axis may be equivalently viewed as a spatial axis. The heights h_0 and h_1 are indicated, and although the atmosphere is continuously stratified, three distinct air masses can still be identified. The shaded region represents the densest air mass, or the density current associated with the dissipating gust front. The stippled region shows the cold air below the inversion (an air mass less dense than the density current). Finally, the white region indicates the least dense, or in this case, the relatively warmer air above the inversion. The bore forms along the interface between the stippled and white regions. However, as the least dense air (white region) interacts with the bore, vertically damped gravity waves are generated above the bore, as indicated by the streamlines.

The structure of the observed atmospheric bore is different than the idealized bores shown in Fig. 2. Notably, the undulations in the observed bore are found behind the initial bore

Schematic of an Observed Bore

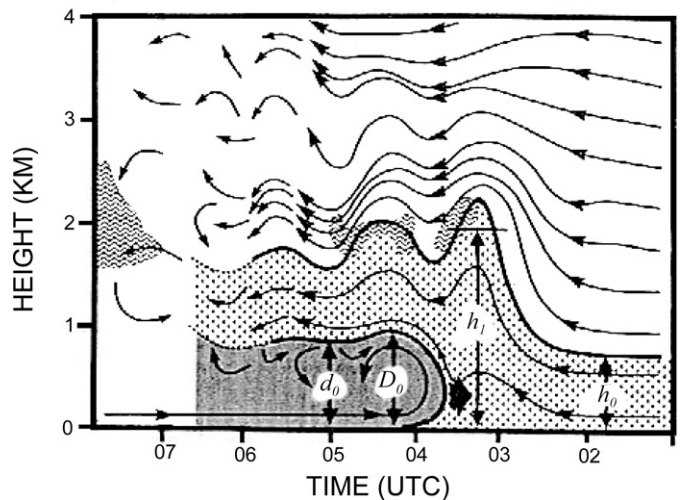


Fig. 5. Schematic of a bore observed on Earth, derived from radiosonde and tower data (adapted from Fig. 18, Koch et al., 1991). The density current (shaded region) from a dissipating thunderstorm gust front generates a bore (stippled region) as the current flows through a less dense atmosphere. The streamlines above the bore show vertically damped gravity waves excited by the bore passage.

disturbance. This difference is a result of the velocity of the undisturbed fluid ahead of the bore, which counters through advection the propagation of the bore wave undulations. Specifically, the unperturbed flow impinging upon the bore front has $Fr > 1$, which indicates that waves triggered at the bore cannot propagate out ahead of the bore. If the undisturbed fluid were motionless, the bore wave undulations would propagate ahead of the bore, as shown in Figs. 2 and 4.

2.2. Martian observations of putative bore wave clouds

Nocturnal inversions (cold, dense air underlying less dense, warmer air) on Mars are conducive for atmospheric bore wave formation. Cold katabatic flows driven by negative thermal buoyancy produced through intense radiative cooling on high topography accelerate down the slopes. Although these flows warm adiabatically with descent, this is offset by radiative cooling during descent, and overall, the flows remain colder than the surrounding environment. Thus, these currents can undercut the local radiation inversion and produce bore waves as suggested by Hunt et al. (1981) and Pickersgill (1984).

Clouds might develop or be enhanced along the rising branch of undular bore waves or at the leading edge of a bore head if the atmosphere is near saturation. Linear and wave-like cloud disturbances were observed northwest of Pavonis Mons, east of Arsia Mons between Pavonis and Ascræus Mons, south of Olympus Mons, and southwest of Arsia Mons (Kahn and Gierasch, 1982). The most well-defined clouds were seen between Pavonis and Arsia Mons (Fig. 1). Wavelengths derived from the Viking images ranged from 10–20 km, with propagation speeds of 6.8–27.6 m/s (Pickersgill, 1984). The waves, made visible by condensation, were also observed to bend and refract around large topographic barriers suggesting the disturbances were confined near the surface (Hunt et al., 1981). The clouds were most evident, based on two-year Viking climatology, between $L_s = 69.8^\circ$ – 121.5° for the first year, and $L_s = 33.6^\circ$ – 121.5° the second year (Pickersgill, 1984). These clouds have not been imaged by Mars Orbiter Camera (MOC) aboard Mars Global Surveyor (MGS), due to the roughly 1400 local time of observations in mapping phase, well beyond the time at which the clouds and the katabatic fronts are expected to dissipate. MOC images taken out of the 1300–1500 local time window during aerobraking show no obvious bore wave-like clouds, but the wide-angle images taken over the Tharsis region during aerobraking maneuvers were taken no earlier than 1100 local time, by which time bores are expected to have dissipated. Also, these aerobraking images were obtained around $L_s = 260^\circ$, when atmospheric water vapor content is near a minimum (Smith, 2004), and thus the formation of clouds from nighttime katabatic flows is not favored. Finally, as discussed in Section 4, if bore waves and/or gravity waves are responsible for generating the clouds, these phenomena are more dynamically favored in the northern hemisphere summer.

3. Model description and simulation design

This study uses the Mars Regional Atmospheric Modeling System (MRAMS) to simulate the nightly katabatic flow. MRAMS was adapted for Mars from a widely used terrestrial modeling code (Pielke et al., 1992). It is a non-hydrostatic model that simulates synoptic-scale, mesoscale, and microscale atmospheric flows over complex topography (e.g., Rafkin et al., 2002; Michaels and Rafkin, 2004; Rafkin and Michaels, 2003; Rafkin et al., 2004). Rafkin et al. (2001) provides a complete description of the model.

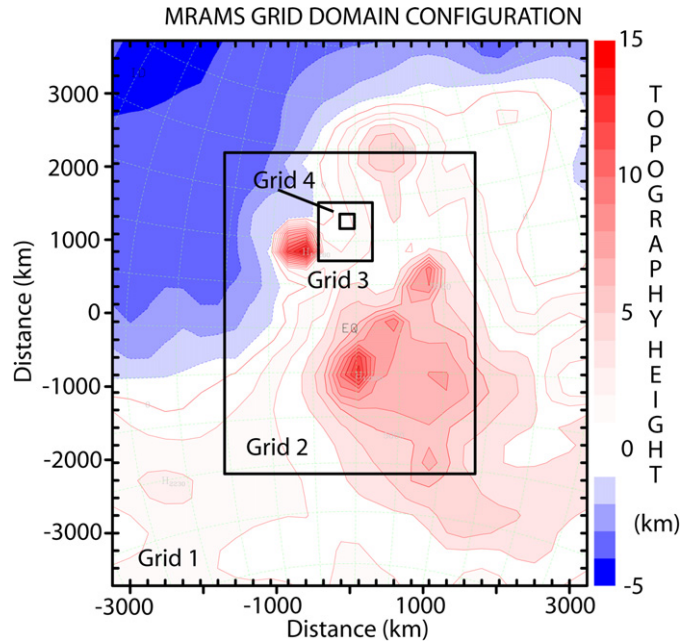


Fig. 6. Topography on the first model grid; the locations of the other three grids are indicated by the boxes. Topography is successively better resolved on each nested grid.

All simulations in this study are configured with four grids (Fig. 6). The first grid has a horizontal grid spacing of 240 km and encompasses the entire Tharsis bulge. This grid is configured to provide a smooth transition to the mesoscale grid spacing from the NASA Ames Mars General Circulation Model (MGCM) (Haberle et al., 1999), which provides initial and boundary conditions. The second grid resolves the bulk of the Tharsis volcanoes and has a 60 km grid-spacing. Nests three and four of these simulations are positioned slightly northeast of Olympus Mons, and have horizontal grid spacing of 15 and 3 km, respectively. Although Viking observations suggest the most well-defined bore-like disturbances are found between Arsia and Pavonis Mons, the locations of the grids in this study were previously selected for an unrelated atmosphere–surface interaction simulation. However, as will be shown, the putative bore waves were well represented within the grid domains covering the flanks of Olympus Mons.

All grids have the same vertical resolution, with vertical grid intervals increasing with height. The lowest model level is at 25 m above the ground, with the maximum interval reaching 3000 m at about 30 km above ground level. There are 60 vertical levels with a model top at approximately 70 km above the areoid. The simulations were run at six solar longitudes: $L_s = 90^\circ$, 142° , 100° , 180° , 270° and 358° , in order to assess seasonal variations. The duration of each simulation was 4 sols (and three nights).

4. Model results

4.1. Katabatic fronts and bore structures

Every night, at all simulated seasons, strong downslope flows originate along the slopes of the four volcanoes, as seen

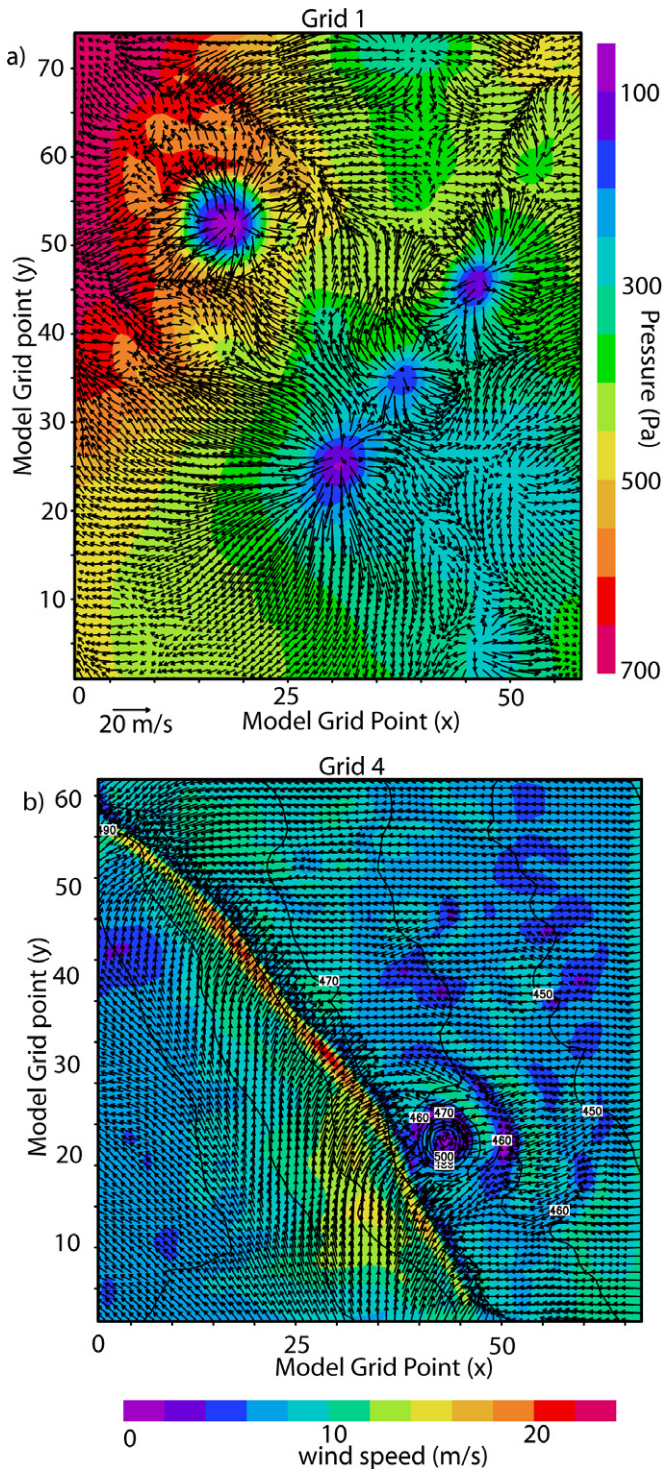


Fig. 7. (a) A horizontal cross-section at a local time at 2317 and $L_s = 100^\circ$ of the near-surface winds (vectors) with pressure (shaded; used as a proxy for topographic height on grid 2) showing the katabatic winds and fronts emanating from the four Tharsis volcanoes. The scale of the 20 m/s velocity vector is indicated in the lower left of the figure panel. The axes are given in terms of model grid points, with ~ 60 km grid spacing per point on this grid. (b) Near-surface wind speed (shaded) and wind vectors as the front passes through the fourth grid domain at 2350 local time at $L_s = 100^\circ$. Pressure (Pa) is contoured as a proxy for topographic height. The crater in the middle of the grid did little to impede the progress of the front. The velocity vector scale is as indicated in (a). The front is identified by a pronounced wind shift and narrow region of winds of 20 m/s and greater. There is ~ 3 km per model grid point on this grid.

in grid 2 (Fig. 7a). Katabatic fronts form at the leading edge of these flows as the dense air from higher elevations accelerate down the volcano slopes and move radially outward. These fronts are observed as soon as the flow changes from upslope to downslope, starting at the top of the volcanoes. As the downslope flow spreads across the plains surrounding the volcanoes, some of the radial symmetry is lost due to local topographic effects and interaction with atmospheric flows from the surrounding volcanoes. The passage of a katabatic front from Olympus Mons is captured in the fourth grid (Fig. 7b). Prevailing winds are easterly ahead of the front. Winds are southerly behind the front, and stay this way well after the front has passed, only to shift again when the sun rises and the flow turns upslope (easterly). The density field (not shown) also shows a denser air mass (0.016 kg/m^3 in the katabatic current vs 0.0145 kg/m^3 in the undisturbed region) as the front first enters the grid.

A vertical cross-section of temperature and potential temperature through the front at $L_s = 100^\circ$ shows three different air masses (Fig. 8a). A shallow, undisturbed layer of radiatively cooled air is found below relatively warm air in the right (eastern) half of the figure. This represents the classical nocturnal inversion scenario, and can be likened to the undisturbed two-layer fluid system seen upstream of the density current seen in Fig. 2. Katabatic flow originating from the slopes of Olympus Mons is very cold and dense, as evidenced in the left (western) half of Fig. 8a. The katabatic front is seen at the center of the figure, forcing the radiatively-cooled nocturnal inversion air up above the katabatic density current. The katabatic density current itself is very shallow, about the same depth as the nocturnal inversion. As the front passes through, the nocturnal inversion deepens as the air is forced over the current. The modeled structure most closely resembles the terrestrial atmospheric bore shown in Fig. 5. Therefore, the modeled phenomenon is, at least morphologically, a bore. As will be shown later, the disturbance also behaves dynamically like a bore, and for this reason, we identify it as such in the remainder of this paper.

Directly behind the front, a mature bore head can be seen detaching from the bulk of the density current, similar to that shown in Fig. 2 at time $t + 2dt$. However, unlike the bore shown in Fig. 2, waves do not propagate ahead of the front, because of an impinging flow in excess of 20 m/s. Without this impinging flow, the velocity seen by the density current would be much less (on the order of a few meters per second), and $Fr \leq 1$. In the present situation, the resulting Fr number is greater than 1, and the waves are advected back over the density current by the impinging current.

The air above the bore is far enough from the surface that effects of radiative cooling from the surface are not dominant and the atmosphere here can be considered adiabatic. Potential temperatures in this region therefore correspond to material surfaces for adiabatic processes and are taken as a proxy for streamlines in this study. This allows comparison of Fig. 8a with observed bore waves on Earth, such as that shown in Fig. 5. In both figures, two kinds of waves are seen: waves associated with the bore itself, and gravity waves that are excited in the air mass above the density current. The bore wave structure evident

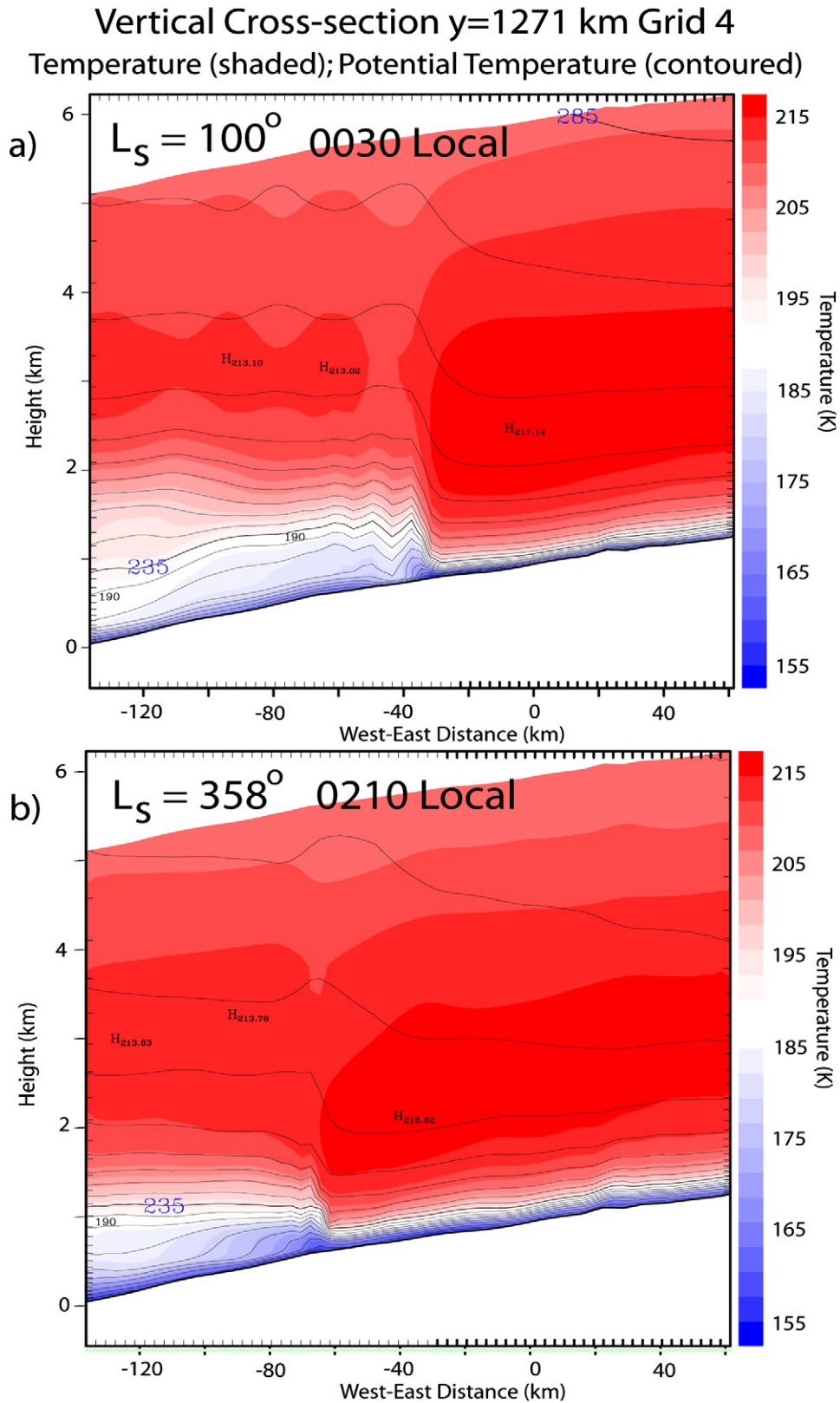


Fig. 8. A vertical cross-section of temperature (shaded) with potential temperature (contours) on grid 4. The location of the cross-section is along model grid point $y = 40$, as shown in Fig. 7. Note that only the lowest 6 km of the vertical domain are displayed. (a) 0030 local time at $L_S = 100^\circ$. The katabatic current from Olympus Mons is coming in from the west (blue shaded colors, roughly) and raises the nocturnal inversion boundary (white shaded colors, roughly) as it passes through. The relatively warmer air aloft is roughly indicated by red shades. The potential temperature contours are considered to be approximately a material surface, and thus indicate streamlines. The undulations in the potential temperature contours associated with the bore damp out with height until they almost flatten out at about 3 km above the ground. Undulations associated with gravity waves start to develop above this height. Compare with Fig. 5. (b) 0210 local time on $L_S = 358$. The current at this season does not generate a strong and defined undular bore, but a single, vertically propagating gravity wave is evident above the front.

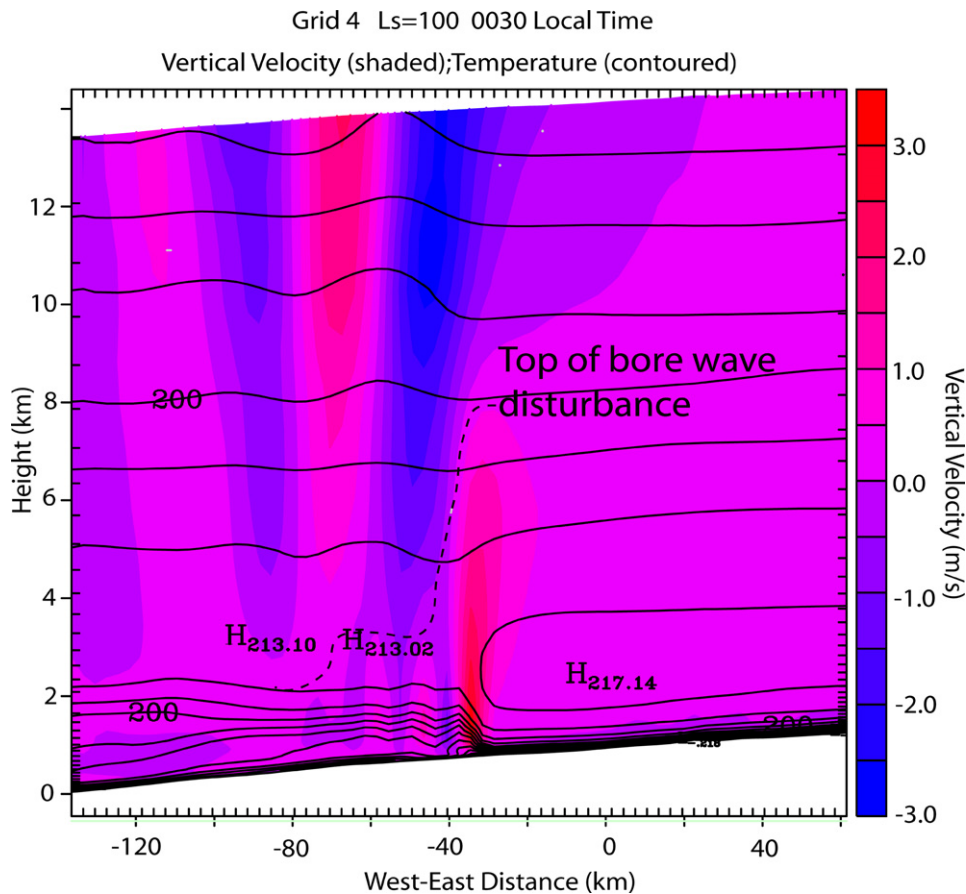


Fig. 9. A vertical cross-section as in Fig. 8a, but of vertical winds (shaded) with temperature contours. The temperature contours show the density current itself is confined very close to the surface and its depth is comparative to that of the inversion height in the undisturbed air. As the current impinges into the undisturbed flow, air is pushed over the current and the inversion height is raised over it. Behind the leading edge of the bore, the ascending/descending winds associated with the bore extend only to about 3 km (as indicated by the dashed line), with distinctly separate gravity waves above. Note that the bore undulations have a shorter horizontal wavelength than the gravity waves, which further distinguishes the two wave disturbances.

in the simulated potential temperature field closely resembles the streamlines seen in Fig. 5. The bore wave disturbance then interacts with the overlying atmosphere and generates either vertically propagating or damped gravity waves. The difference in propagation behavior is a result of differences in atmospheric structure, i.e., in the Scorer parameter (see Section 4.2).

When the bore is well defined in the simulations, gravity waves triggered by the bore propagate vertically in the lowest scale height of the atmosphere (Fig. 9). Perturbations associated with the gravity waves reach maximum amplitude at an altitude of approximately 20 km above the surface, then gradually damp with height until they are no longer identifiable at an altitude of approximately 40 km. Bore wave undulations behind the front are well defined up to ~ 3 km above the surface before damping out. The vertical winds at the leading edge of the bore extend much higher than the undulations of the bore wave, up to ~ 9 km, because winds here constructively interfere with the leading edge of the gravity waves above the bore. It is likely that the bore waves are what generate the rolling type of clouds observed by the Viking Orbiters, rather than the gravity waves, because the simulated bore waves are found closer to the ground, and the observed waves appear as perturbations on

a low cloud (Hunt et al., 1981). Moreover, the distance between ascending branches of the simulated bore undulations is about 12 km; this falls into the lower wavelength range (10–20 km) of the wave clouds measured by Hunt et al. (1981). The gravity wave wavelength is ~ 50 km, which is much larger than the wavelength observed in the Viking cloud images.

4.2. Seasonal behavior

Although katabatic flows occur every night throughout the year, undulations are not found in all simulations. Bore waves are simulated at $L_s = 90^\circ$, become more pronounced at $L_s = 100^\circ$, and weaken, but are still seen at $L_s = 142^\circ$. During the other simulated seasons, $L_s = 180^\circ$, 270° , and 358° , the katabatic current does not appear to excite the same strong gravity or undular bore wave-like behavior. Fig. 8b shows the katabatic flow at $L_s = 358^\circ$. Although similar in appearance to a turbulent bore (refer to Fig. 4c), the ratio of the hump height (h_1) to the depth of the undisturbed inversion (h_0) does not exceed 4, which is the criterion that characterizes turbulent bores. This singular hump at the head of the katabatic current is more similar to the usual disturbance associated with a front, where there is a slight build up of dense fluid behind the front as it converges

with the undisturbed, less dense air. A single, low amplitude gravity wave forms aloft as air is forced up by the passing front.

Based on model results, the bore strength (h_1/h_0) is approximately 3.7 at $L_s = 100^\circ$. In comparison, the strength is 2.8 at $L_s = 142^\circ$ and 3.1 at $L_s = 90^\circ$. The fastest bores were seen at $L_s = 90^\circ$ and 100° , with the disturbance traveling at about 20 m s^{-1} (relative to the ground). At $L_s = 142^\circ$, the bore had a speed of approximately 17 m s^{-1} . These model-predicted speeds can be compared with Eq. (2), which gives 22 m s^{-1} for $L_s = 100^\circ$, 20 m s^{-1} for $L_s = 142^\circ$, and 21 m s^{-1} for $L_s = 90^\circ$. The theoretical speeds compare relatively well to those predicted by the model. It takes the bore 2.5 h to cross the fourth grid at the strongest seasons. The bore strengthens (i.e., its depth increases) during the first hour, and then slowly weakens as it travels up the slight slope. The bore generally appears in the grid by 2330 local time, but it appears about an hour later during the weaker seasons, with the front dissipating before it can cross the domain.

Vertically propagating gravity waves are also evident during the stronger seasons. At the other three seasons ($L_s = 180^\circ$, 270° , and 358°), there is little indication of any vertical wave propagation. A possible explanation for this is found in the structure of the atmosphere during these seasons. One way of examining the atmospheric vertical structure is via the Scorer parameter, and this was calculated for two seasons: $L_s = 100^\circ$ and 358° .

The Scorer parameter (l^2) determines the vertical propagation characteristics of linear gravity waves. It combines the effects of both the stability and the vertical wind profile, and is expressed as

$$l^2(z) = \frac{N^2(z)}{U^2(z)} - \frac{1}{U(z)} \frac{\partial^2 U}{\partial z^2}, \quad (4)$$

where N^2 is the Brunt–Vaisala frequency,

$$N^2 = \frac{g}{\theta} \frac{\partial \theta}{\partial z}. \quad (5)$$

U is horizontal wind component in the plane of the gravity wave, and θ is potential temperature. The second term on the r.h.s. of (4) can be important if there is substantial curvature of the wind profile, or if the wind speed is small. The Scorer wavelength is $\lambda_l = 2\pi/l$. Gravity waves with horizontal wavelengths greater than this value will propagate vertically, while wavelengths less than λ_l will damp with height.

The stability of the atmosphere at both seasons is similar, but the vertical east–west wind profiles are not (Fig. 10). The winds are easterly nearest the surface, with a layer of westerlies above in the weak ($L_s = 358^\circ$) bore case (Fig. 10b). Above that, the winds shift once more to easterlies. Also, compared to $L_s = 100^\circ$ (Fig. 10a), there is a relatively deep region of weak winds at $L_s = 358^\circ$ between 2 and 8 km. The differences in the u-wind vertical structures result in different λ_l profiles for each season (Fig. 11). The Scorer wavelengths are limited to relatively small wavelengths, never exceeding ~ 7 km in the $L_s = 100^\circ$ simulation. Thus the ~ 50 km wavelength gravity waves seen in the simulation are able to propagate. At $L_s = 358^\circ$, the λ_l profile has higher values, with several regions

where λ_l is imaginary (i.e., the Scorer parameter is negative, and/or the Scorer wavelength is infinite), as indicated by discontinuities in the profile shown in Fig. 11. Imaginary values indicate critical layers through which no gravity waves of any wavelength may propagate. The single gravity wave excited immediately above the katabatic front at $L_s = 358^\circ$ damps out below an altitude of ~ 6 km, which is consistent with the Scorer parameter profile.

The seasonality of the phenomenon predicted by the model coincides with the Viking observations, where bore wave clouds were only seen during late northern spring and early northern summer ($L_s = 33.6^\circ$ at the earliest to $L_s = 121.5^\circ$ at the latest). Though the model results are from Olympus Mons, they are comparable with observational data from the wave clouds seen near, and between, Pavonis and Arsia Mons. The observed typical propagation speed for the bore waves near these volcanoes was $6.8\text{--}27.6 \text{ m s}^{-1}$ (Pickersgill, 1984) and the clouds were believed to form near the surface.

The clouds were also observed in the early morning hours, and although the model results show the bore appearing in the fourth grid near midnight, the timing of the observations can still be explained. During the summer season, the bore maintains its structure as it crosses grid 4, and is still seen moving through the plains in grid 2 during the early morning hours. By the time the Sun has risen, upslope flow begins to develop along the volcano flanks, but this does not affect the bore immediately as it has traveled far enough away from the volcanoes at this time. This allows for the formation of wave clouds throughout the early morning.

Aside from the simulated seasonal atmospheric dynamics, the appearance of the wave clouds is strongly related to the amount of water vapor in the atmosphere. The amount of water clouds observed over Tharsis by MOC, and water vapor by Viking Mars Atmospheric Water Detector and the Thermal Emission Spectrometer (TES) aboard MGS show this. TES observations (Smith, 2004) show water vapor originating from the exposed northern water ice cap during late northern spring and early summer, migrating to the tropics throughout the summer. The aphelion cloud belt, formed by the cross-equatorial Hadley circulation, is also seen in the observations at these same seasons. Simulations by MGCMS (Montmessin et al., 2004; Richardson et al., 2002; Houben et al., 1997) also demonstrate that the tropical air is most moist during the summer. This relatively high concentration of water vapor in the atmosphere, coupled with the seasonal dynamics, make the conditions conducive for allowing the presence of bore waves to be manifested as long wave clouds.

Finally, the lack of bores during some seasons can be explained by examining the ratio between the density current height and h_0 . Although it was difficult to identify distinct layers and distinguish the actual density current in a continuously stratified atmosphere, the two heights were roughly estimated from the model results. It was found that at $L_s = 358^\circ$, h_0 was greater than the density current height; it was the opposite for $L_s = 100^\circ$. This implied that the flow was likely partially or completely blocked at $L_s = 100^\circ$, and supercritical at $L_s = 358^\circ$. These flow regimes are indicated on Fig. 3—the

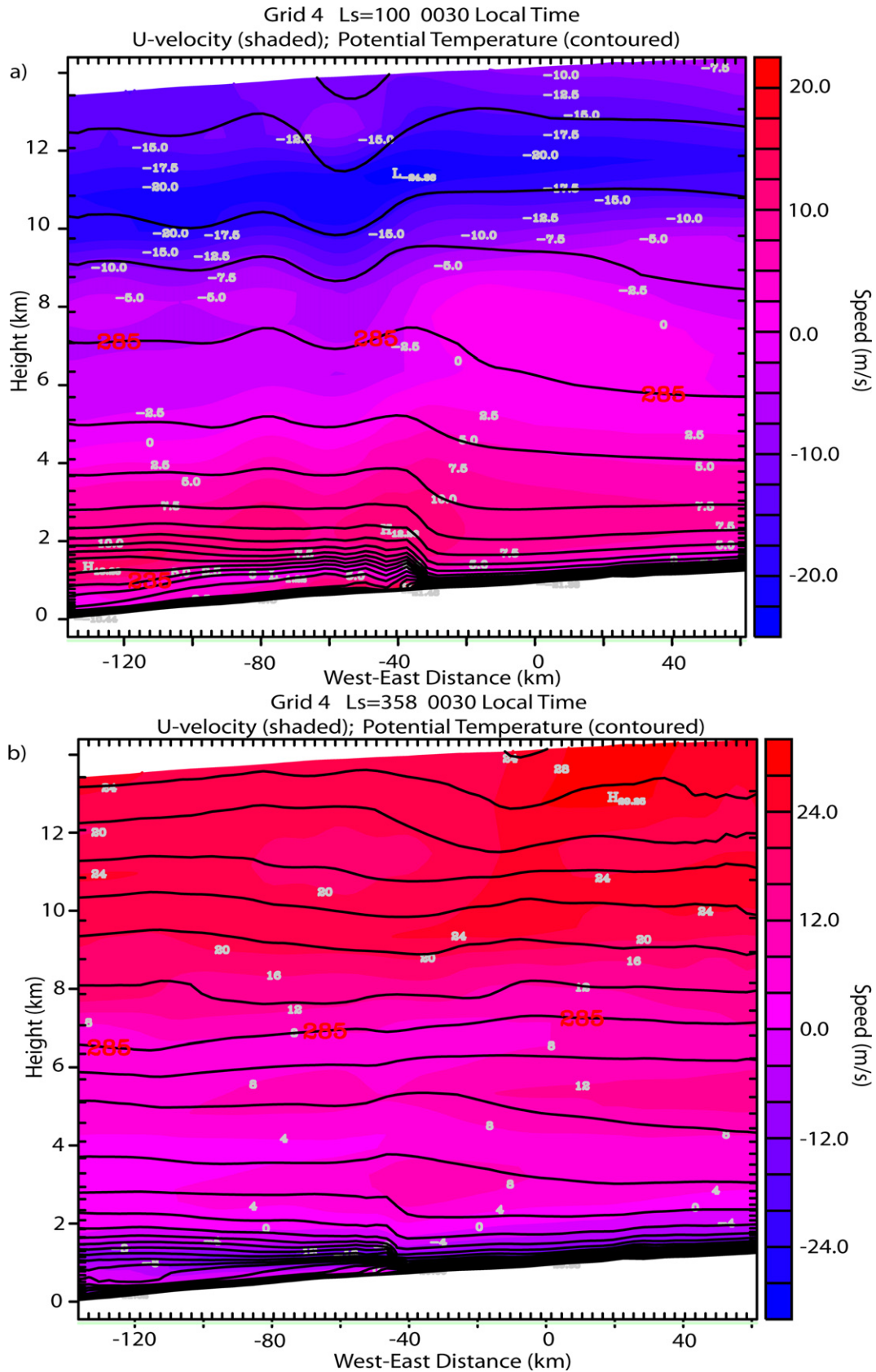


Fig. 10. Vertical cross-section of east-west winds (shaded) with potential temperature contours. Westerly winds are in red, easterly are in blue. (a) At $L_s = 100^\circ$, the layer of easterlies are very shallow, confined to less than a kilometer above the ground. (b) At $L_s = 358^\circ$, the layer of easterlies are deeper than at $L_s = 100^\circ$, extending to almost 2 km above the surface. The extremely shallow westerlies associated with the katabatic current are capped by the easterly winds.

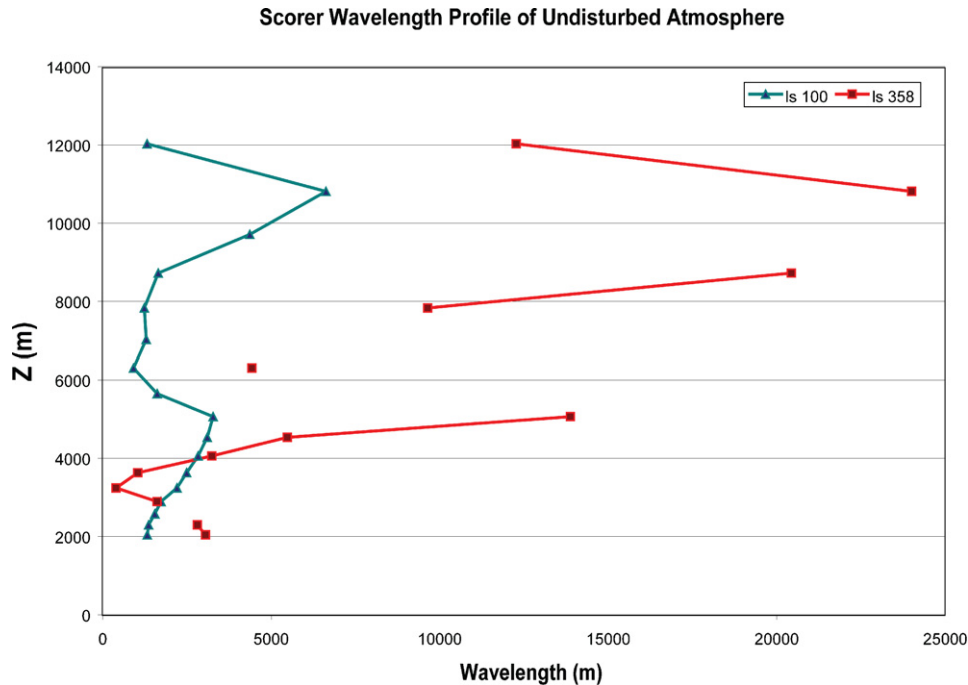


Fig. 11. The Scorer wavelength profile at $L_s = 100^\circ$ and $L_s = 358^\circ$. The Scorer wavelength values for northern summer are smaller, and thus, the range of wavelengths over which gravity waves are allowed to propagate is larger.

filled dot shows the approximate regime at $L_s = 100^\circ$, and the open dot is for $L_s = 358^\circ$. Based on hydraulic theory, bores form when the flow is partially or completely blocked.

5. Summary and conclusions

Nightly katabatic winds off the Tharsis volcanoes form atmospheric bore waves that match long, linear clouds observed by the Viking Orbiters. There is seasonality to the bore waves, which only developed along katabatic fronts during $L_s = 90^\circ$, 100° , and 142° . These seasons were particularly conducive for bore wave formation because of the vertical structure of the lowest 1000 m of the atmosphere, where the ratio of the density current depth and h_0 was greater than 1, characterizing the flow as partially or completely blocked. Vertically propagating gravity waves are more easily generated in the summer when the vertical structure of the atmosphere, as measured by the Scorer parameter, is favorable. The strong ascending and descending winds associated with the bore, rather than the gravity waves above the bore, appear to be what generates the observed linear, smoothly rolling clouds. The seasonality of atmospheric water vapor abundance in this region is also a major factor in the absence of clouds during the other seasons.

The bore phenomenon is strongly associated with topographically-driven katabatic fronts, and thus the same disturbance can be expected (as long as a conducive atmospheric environment exists) along the flanks and nearby plains of other volcanoes and steep topography. The results of this study support the hypothesis that atmospheric bore waves in the Tharsis region produce the wave-like clouds observed by Viking.

Future work on this subject would greatly benefit from the acquisition of additional observations during the morning

hours. Mars Express, the Mars Climate Orbiter, and MTO (assuming it carries a suitable camera), may be able to provide these images. Thermal imaging during the night would be extremely valuable, but would require instrumentation sensitive enough to separate the low level temperature signal from the underlying ground, as well as the temperature differences between the adjacent air masses. Spacecraft observations with large horizontal footprints, such as would be obtained by limb sounders would likely not capture the temperature/density discontinuities; nadir pointing instruments are probably best suited for this task.

Acknowledgments

We thank Drs. Mark Bullock, Jeff Hollingsworth, Robert Haberle, and Tony Colaprete for their careful reviews and input which greatly improved this paper. This project was funded by the NASA Mars Data Analysis Program (NAG5-13376) and the NASA Planetary Atmosphere Program (NAG5-9751).

References

- Briggs, G., Klaasen, K., Thorpe, T., Wellman, J., Baum, W., 1977. Martian dynamical phenomena during June–November 1976—Viking Orbiter imaging results. *J. Geophys. Res.* 82, 4121–4149.
- Clarke, R.H., 1972. The Morning Glory: An atmospheric hydraulic jump. *J. Appl. Meteor.* 11, 304–311.
- Haberle, R.M., Joshi, M.M., Murphy, J.R., Barnes, J.R., Schofield, J.T., Wilson, G.W., Lopez-Valverde, M., Hollingsworth, J.L., Bridger, A.F.C., Schaeffer, J., 1999. General circulation model simulations of the Mars Pathfinder atmospheric structure investigation/meteorology data. *J. Geophys. Res.* 104, 8957–8974.
- Holyer, J.Y., Huppert, H.E., 1980. Gravity currents entering a two-layer fluid. *J. Fluid. Mech.* 100, 739–767.

- Houben, H., Haberle, R.M., Young, R.E., Zent, A.P., 1997. Modeling the martian water cycle. *J. Geophys. Res.* 102, 9069–9084.
- Houghton, D.D., Kasahara, A., 1968. Nonlinear shallow fluid flow over and isolated ridge. *Commun. Pure Appl. Math.* 21, 1–23.
- Hunt, G.E., Pickersgill, A.O., James, P.B., Evans, N., 1981. Daily and seasonal Viking observations of martian bore wave systems. *Nature* 293, 630–633.
- Huppert, H.E., Simpson, J.E., 1980. The slumping of gravity currents. *J. Fluid Mech.* 99, 785–799.
- Kahn, R., Gierasch, P., 1982. Long cloud observations on Mars and implications for boundary layer characteristics over slopes. *J. Geophys. Res.* 87, 867–880.
- Klemp, J.B., Rotunno, R., Skamarock, W.C., 1997. On the propagation of internal bores. *J. Fluid Mech.* 331, 81–106.
- Koch, S.E., Dorian, P.B., Ferrare, R., Melfi, S.H., Skillman, W.C., Whiteman, D., 1991. Structure of an internal bore and dissipating gravity current as revealed by Raman lidar. *Mon. Weather Rev.* 119, 857–887.
- Michaels, T.I., Rafkin, S.C.R., 2004. Large eddy simulation of the convective boundary layer of Mars. *Quart. J. R. Meteor. Soc.* 130, 1251–1274.
- Montmessin, F., Forget, F., Rannou, P., Cabane, M., Haberle, R.M., 2004. Origin and role of water ice clouds in the martian water cycle as inferred from a general circulation model. *J. Geophys. Res.* 109, doi:10.1029/2004JE002284.
- Pickersgill, A.O., 1984. Martian bore waves of the Tharsis region: A comparison with Australian atmospheric waves of elevation. *J. Atmos. Sci.* 41, 1461–1473.
- Pielke, R.A., coauthors, 1992. A comprehensive meteorological modeling system—RAMS. *Meteor. Atmos. Phys.* 49, 69–91.
- Rafkin, S.C.R., Michaels, T.I., 2003. Meteorological predictions for 2003 Mars Exploration Rover high-priority landing sites. *J. Geophys. Res.* 108, doi:10.1029/2002JE002027.
- Rafkin, S.C.R., Haberle, R.M., Michaels, T.I., 2001. The Mars regional atmospheric modeling system: Model description and selected simulations. *Icarus* 151, 228–256.
- Rafkin, S.C.R., Michaels, T.I., Haberle, R.M., 2004. Meteorological predictions for the Beagle 2 mission to Mars. *Geophys. Res. Lett.* 31, doi:10.1029/2003GL018966.
- Rafkin, S.C.R., Sta. Maria, M.R.V., Michaels, T.I., 2002. Simulation of the atmospheric thermal circulation of a martian volcano using a mesoscale numerical model. *Nature* 419, 697–698.
- Richardson, M.I., Wilson, R.J., Rodin, A.I., 2002. Water ice clouds in the martian atmosphere: General circulations model experiments with a simple cloud scheme. *J. Geophys. Res.* 107, doi:10.1029/2001JE001804.
- Rottman, J.W., Simpson, J.E., 1989. The formation of internal bores in the atmosphere: A laboratory model. *Quart. J. R. Meteor. Soc.* 115, 941–963.
- Smith, M.D., 2004. Interannual variability in TES atmospheric observation of Mars during 1999–2003. *Icarus* 167, 148–165.